


# Atomic-level quantitative analysis of electronic functional materials by aberration-corrected STEM

Wanbo Qu(曲万博), Zhihao Zhao(赵志昊), Yuxuan Yang(杨宇轩), Yang Zhang(张杨), Shengwu Guo(郭生武), Fei Li(李飞), Xiangdong Ding(丁向东), Jun Sun(孙军), and Haijun Wu(武海军)

**Citation:**Chin. Phys. B, 2024, 33 (**11**): 116802. DOI: 10.1088/1674-1056/ad7afc
Journal homepage: http://cpb.iphy.ac.cn; http://iopscience.iop.org/cpb

**What follows is a list of articles you may be interested in**

---

## Effect of surface modification on the radiation stability of diamond ohmic contacts

Lian-Xi Mu(牟恋希), Shang-Man Zhao(赵上熳), Peng Wang(王鹏), Xiao-Lu Yuan(原晓芦), Jin-Long Liu(刘金龙), Zhi-Fu Zhu(朱志甫), Liang-Xian Chen(陈良贤), Jun-Jun Wei(魏俊俊), Xiao-Ping Ou-Yang(欧阳晓平), and Cheng-Ming Li(李成明)

Chin. Phys. B, 2024, 33 (**2**): 026801. DOI: 10.1088/1674-1056/ace61e

## Visualizing interface states in $In_2Se_3$–$WSe_2$ monolayer lateral heterostructures

Da Huo(霍达), Yusong Bai(白玉松), Xiaoyu Lin(林笑宇), Jinghao Deng(邓京昊), Zemin Pan(潘泽敏), Chao Zhu(朱超), Chuansheng Liu(刘传胜), and Chendong Zhang(张晨栋)

Chin. Phys. B, 2023, 32 (**5**): 056803. DOI: 10.1088/1674-1056/acbaef

## Polarization Raman spectra of graphene nanoribbons

Wangwei Xu(许望伟), Shijie Sun(孙诗杰), Muzi Yang(杨慕紫), Zhenliang Hao(郝振亮), Lei Gao(高蕾), Jianchen Lu(卢建臣), Jiasen Zhu(朱嘉森), Jian Chen(陈建), and Jinming Cai(蔡金明)

Chin. Phys. B, 2023, 32 (**4**): 046803. DOI: 10.1088/1674-1056/ac80b3

## Quantitative HRTEM and its application in the study of oxide materials

Chun-Lin Jia(贾春林), Shao-Bo Mi(米少波), Lei Jin(金磊)

Chin. Phys. B, 2018, 27 (**5**): 056803. DOI: 10.1088/1674-1056/27/5/056803

## Adsorption of glycine on diamond (001): Role of bond angle ofcarbon atoms

Li Lin (李林), Xu Jing (徐靖), Xu Li-Fang (徐力方), Lian Chao-Sheng (廉朝胜), Li Jun-Jie (李俊杰), Wang Jian-Tao (王建涛), Gu Chang-Zhi (顾长志)

Chin. Phys. B, 2015, 24 (**5**): 056803. DOI: 10.1088/1674-1056/24/5/056803

---

**TOPICAL REVIEW — Stephen J. Pennycook: A research life in atomic-resolution STEM and EELS**

# Atomic-level quantitative analysis of electronic functional materials by aberration-corrected STEM

Wanbo Qu(曲万博)[1], Zhihao Zhao(赵志昊)[1], Yuxuan Yang(杨宇轩)[1], Yang Zhang(张杨)[1,2,3,†], Shengwu Guo(郭生武)[1], Fei Li(李飞)[1,2], Xiangdong Ding(丁向东)[1], Jun Sun(孙军)[1], and Haijun Wu(武海军)[1,‡]

[1] *State Key Laboratory for Mechanical Behavior of Materials, Xi'an Jiaotong University, Xi'an* 710049, *China*
[2] *Electronic Materials Research Laboratory, Key Laboratory of the Ministry of Education, and School of Electronic and Information Engineering, Xi'an Jiaotong University, Xi'an* 710049, *China*
[3] *Instrumental Analysis Center of Xi'an Jiaotong University, Xi'an Jiaotong University, Xi'an* 710049, *China*

(Received 9 July 2024; revised manuscript received 27 August 2024; accepted manuscript online 14 September 2024)

The stable sub-angstrom resolution of the aberration-corrected scanning transmission electron microscope (AC-STEM) makes it an advanced and practical characterization technique for all materials. Owing to the prosperous advancement in computational technology, specialized software and programs have emerged as potent facilitators across the entirety of electron microscopy characterization process. Utilizing advanced image processing algorithms promotes the rectification of image distortions, concurrently elevating the overall image quality to superior standards. Extracting high-resolution, pixel-level discrete information and converting it into atomic-scale, followed by performing statistical calculations on the physical matters of interest through quantitative analysis, represent an effective strategy to maximize the value of electron microscope images. The efficacious utilization of quantitative analysis of electron microscope images has become a progressively prominent consideration for materials scientists and electron microscopy researchers. This article offers a concise overview of the pivotal procedures in quantitative analysis and summarizes the computational methodologies involved from three perspectives: contrast, lattice and strain, as well as atomic displacements and polarization. It further elaborates on practical applications of these methods in electronic functional materials, notably in piezoelectrics/ferroelectrics and thermoelectrics. It emphasizes the indispensable role of quantitative analysis in fundamental theoretical research, elucidating the structure–property correlations in high-performance systems, and guiding synthesis strategies.

**Keywords:** AC-STEM, quantitative analysis, polarization, electronic functional materials

**PACS:** 68.37.Ma, 06.60.–c, 77.22.Ej, 77.84.–s **DOI:** 10.1088/1674-1056/ad7afc

## 1. Introduction

Advancements in microscopy technology continue to deepen our understanding of the micro world. The scanning transmission electron microscope (STEM) serves as a powerful tool for characterizing materials from nano to atomic scales, combining the characteristics of scanning electron microscopy with those of transmission electron microscopy. As early as 1938, the world's first STEM was developed under the leadership of Manfred von Ardenne at Siemens in Germany. Regrettably, the outbreak of World War II impeded further research, culminating in the unfortunate destruction of the apparatus during an aerial bombardment. In the subsequent decades, progress in this technology stagnated. It was not until 1970 that, thanks to the successful development of field emission electron guns and the appearance of high-quality objective lenses, Albert Crewe's team at the University of Chicago capitalized on STEM to pioneer the groundbreaking direct observation of individual atoms for the first time.[1] In 1991, Pennycook *et al.* at Oak Ridge National Laboratory employed STEM to capture high-resolution high-angle annular dark-field (HAADF) images of low-index crystallographic zones in $YBa_2Cu_3O_{7-x}$ and $ErBa_2Cu_3O_{7-x}$ compounds.[2] This marked a turning point where STEM imaging genuinely achieved atomic resolution. In recent years, the introduction of aberration correction technology has made it possible to achieve sub-atomic electron probes and sub-angstrom spatial resolution imaging. Aberration-corrected scanning transmission electron microscopy (AC-STEM) has gradually matured into an advanced characterization technique capable of simultaneously acquiring multiple images and spectra, enabling precise atomic imaging and mapping of both chemical species and electronic configurations. It has found broad applications in the investigation of a myriad of material systems.

Electronic functional materials encompass a broad and diverse range of materials that play a critical role in modern electronic technologies. These materials typically exhibit unique electrical, magnetic, optical, or thermal properties. Their classification is extensive and includes conductive metals and their alloys, semiconductor materials, dielectric materials, superconducting materials, piezoelectric/ferroelectric materials, magnetic materials, optoelectronic materials, thermoelectric

†Corresponding author. E-mail: zhangyang2020@xjtu.edu.cn
‡Corresponding author. E-mail: wuhaijunnavy@xjtu.edu.cn

© 2024 Chinese Physical Society and IOP Publishing Ltd 

materials, organic electronic materials, etc. They are widely used in various electronic devices and systems, including computer chips, displays, solar cells, fiber optic communication systems, sensors, capacitors, high-frequency circuits, and temperature control systems. Given their impact on technological revolutions, national security, social welfare, economic contributions, and environmental protection, research on the theoretical mechanisms, structural characterization, performance optimization, and process improvement of electronic functional materials garners substantial attention. The emergence of AC-STEM has profound implications for the study of electronic functional materials, primarily manifested in several key aspects. Firstly, the sub-angstrom spatial resolution of AC-STEM enables direct observation of the atomic arrangement within materials. Combined with techniques such as energy dispersive spectroscopy (EDS) and electron energy loss spectroscopy (EELS), this facilitates precise analysis of trace elements and band structures, which is fundamental to understanding the intrinsic properties of electronic functional materials. Secondly, the visualization of surfaces, interfaces, and internal defects helps in evaluating synthesis conditions and revealing the microscale origins of material performance. Lastly, the specific characterization requirements of certain electronic functional materials can be met with AC-STEM, such as using *in situ* techniques and high-speed imaging to study dynamic processes, employing multiscale analysis to investigate the hierarchical structure's impact on overall performance, and utilizing quantitative analysis to determine critical structural parameters and uncover deep-seated rules. In this work, piezoelectric/ferroelectric ceramics/films and thermoelectric semiconductors, as key branches of electronic functional materials, will be discussed as primary representatives.

STEM possesses the remarkable capability to concurrently and in parallel record various signal types across various spatial resolutions. However, due to inherent characteristics such as channeling effects in samples and the lengthy sequential acquisition time required for electron scanning probe imaging, as well as external environmental or instrumental factors like acoustic, mechanical, and electromagnetic disturbances, and inappropriate states resulting from adjustable microscope parameters such as focus, tilt, aperture size and acceleration voltage, the final imaging results inevitably deviate from reality. These factors cannot be overlooked. For instance, channeling effects cause the incident electron beam to propagate preferentially along specific lattice directions rather than randomly, leading to an intensity distribution that does not accurately represent the true nature of the sample. Defocus results in blurred images, impairing the resolution of structural details, while local tilts degrade image quality, which can be detrimental to the accurate reconstruction of three-dimensional structures. Deviations caused by these factors are collectively referred to as image distortion. The issues of serial acquisition artifacts can be broadly categorized into three types: image drift, scan distortion, and scan noise, differentiated by the frequency intervals involved.[3] Image drift refers to easily identifiable image distortion that occurs between a series of frames. These translation offsets are typically caused by stage or sample movements based on factors like thermal expansion and electrical conductivity. Image drift can be corrected through techniques such as frame averaging and alignment with the analysis of time-series data or focal-series data. Low-frequency scan distortion manifests as additional image transformations within each frame, including affine transformations (i.e., image stretching, skewing, shearing, or slight rotations) and non-linear distortions (i.e., straight lattice becoming wavy). These local interferences require correction through rigid or non-rigid registrations. Scan noise, on the other hand, is caused by instability above kilohertz frequencies, typically manifested in images as torn, sliced, or sheared atomic features, with white vertical stripes observable in their Fourier transformations generated from low-order points. Besides careful calibration of instrument parameters and selection of appropriate sample preparation methods, customizing various image processing methods tailored to the frequency range of the distortion is essential for correcting the distortion and generating high-quality images with no drift, no background noise or artifacts, and with enhanced contrast.[3–7] Figure 1 demonstrates the application effects of several image processing methods, including Bragg filter (selecting specific spots in the power spectrum as lattice basis vectors and performing inverse Fourier transform to reduce noise),[4,5] scan-line noise correction (removing horizontal/vertical artifacts from beam deflections due to external fields or hysteresis effects during the 'fly back' between scan lines),[4,5] scan-noise compensation (achieving horizontal (fast-scan) direction reconstruction through iterative comparison of adjacent row image data and vertical (slow-scan) direction reconstruction through reordering of local scan lines),[6] and the removal of planar ramp background (eliminating secondary overall range non-uniformity from sample thickness and local tilt to highlight important local contrast variations).[3]

Following the series of image processing steps such as peak finding and Gaussian fitting, we obtain raw data comprising atomic column positions along with contrast information, which serves as the fundamental basis for subsequent quantitative analyses. Upon the exhaustive acquisition of real-space atomic image data, quantitative analysis proceeds to refine this information to the lattice level, enabling the calculation and statistical analysis of various interesting physical quantities. These encompass aspects such as contrast (distribution of contrast and statistical analysis of chemical ordering), lattice properties (lattice or sub-lattice constants and angles, bond

lengths and angles, specific spacings, and statistical measures of structural ordering including oxygen octahedral tilting and distortion), strain (atomic strain analysis and geometric phase analysis), atomic displacements and polarization (polarization vector maps, quadrant diagrams, domain wall localization and statistical scrutiny of domain wall angles), among other rich dimensions, all of which will be discussed in detail in the following sections.

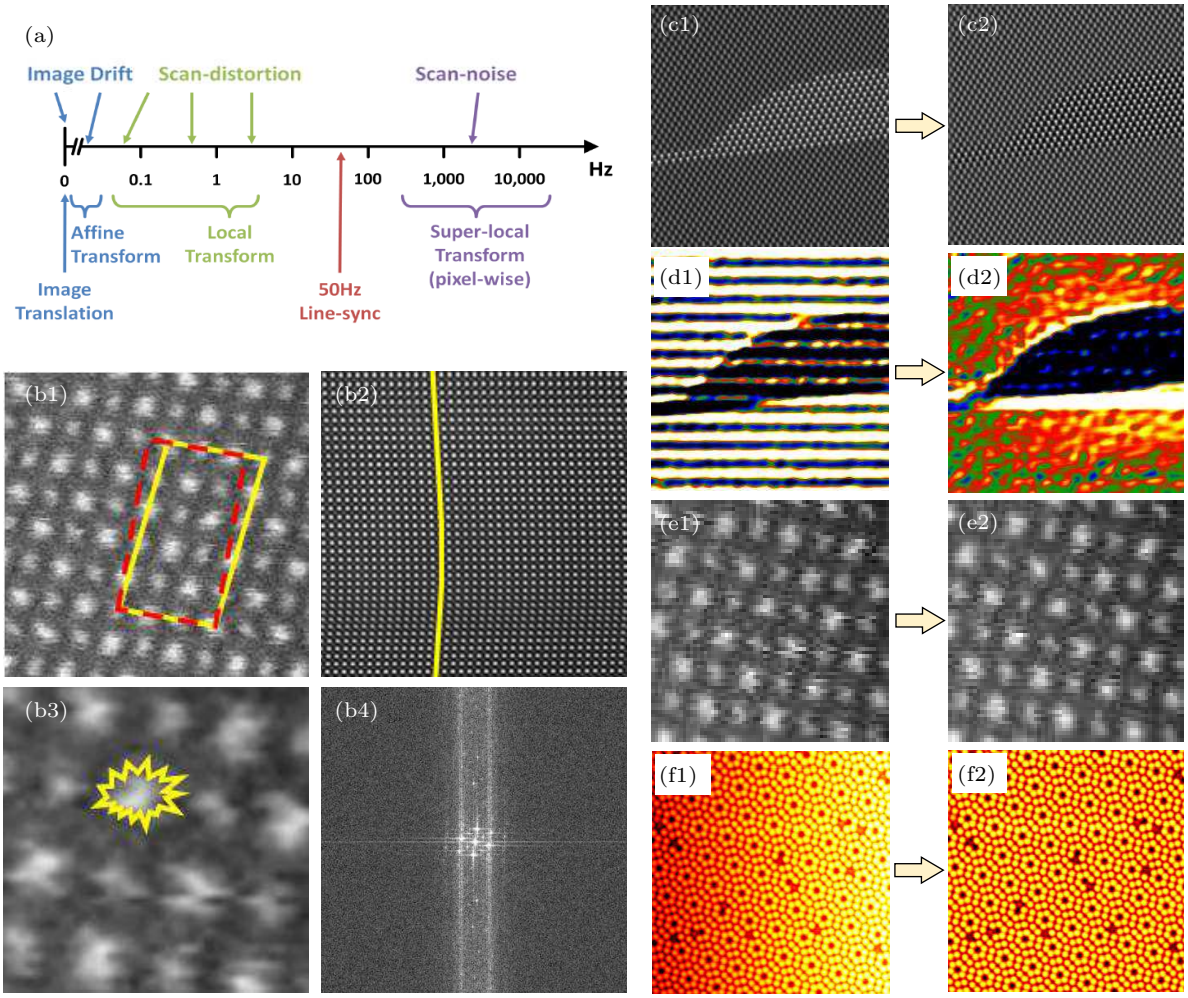



**Fig. 1.** Image distortion and image processing technique in electron microscope. (a) Scanned image artifact types, frequency ranges and remedies. Reproduced with permission.[3] Copyright 2015, Jones *et al.* (b) Several common types of image distortions: (b1) affine transformation, (b2) nonlinear distortion, and (b3)–(b4) scan noise in real space and reciprocal space. Reproduced with permission.[6] Copyright 2013, Microscopy Society of America. (c)–(f) Several types of effective image processing methods: (c1)–(c2) Bragg filter, (d1)–(d2) scan-line (fly-back) noise correction, (e1)–(e2) scan-noise compensation, and (f1)–(f2) the removal of planar ramp background. Reproduced with permission.[8] Copyright 2008–2022, HREM Research Inc (Japan) and Universidad de Cádiz (Spain). Reproduced with permission.[6] Copyright 2013, Microscopy Society of America. Reproduced with permission.[9] Copyright 2015–2021, HREM Research Inc.

## 2. Quantitative analysis of electronic functional materials

### 2.1. Contrast analysis

Contrast signifies the variation in brightness observed across distinct regions of an image. In STEM images, contrast is predominantly determined by the imaging depth (essentially proportional to the atom count within an atomic column) and the atomic number (with HAADF intensity being approximately proportional to $Z^2$ and ABF (annular bright-field) intensity to $Z^{1/3}$, where $Z$ represents the atomic number). The robust correlation between HAADF images and the atomic number $Z$, reflecting its elemental sensitivity, makes it particularly adept at characterizing substitutional dopants within materials. For instance, in thermoelectric semiconductors such as SnS and SnSe,[10,11] fluctuations in contrast irregularities (e.g., anomalous bright spots) can signify substitution among chalcogen elements. Atomic-scale observations of alloying substitutional dopants are pivotal evidence in explaining how crystal structure modifications boost the power factor, diminish lattice thermal conductivity, and consequently elevate the figure of merit ($ZT$ value). When it comes to relaxor ferroelectrics like PMN-PT,[12] disparities in the contrast standard deviations between rare-earth doped samples and their undoped counterparts, as well as between $A$-site and $B$-site in perovskite structures ($ABO_3$), confirm the substitutive nature of doping and pinpoint the substitution locations.

This serves as the microscopic foundation for the substantial piezoelectric performance generated through local structural heterogeneity. With a constant elemental composition (i.e., a fixed $Z$ value) and uniform sample thickness, fluctuations in the contrast of HAADF images effectively indicate the variation in atom counts within atomic columns, thereby providing a means to delineate the presence and spatial distribution of vacancies. In the strengthening work of $Sb_2Te_3$-based thermoelectric alloys through twin engineering,[13] leveraging the positive correlation between image contrast and atom counts within columns allows for the identification of lower contrast regions adjacent to twin boundaries, suggesting the aggregation of Te vacancies. Furthermore, the presence of interstitial atoms near twin boundaries is directly visualized, and owing to the enhanced strain effect, they manifest more pronounced contrast in ABF imaging. Both the interstitial atoms situated along twin boundaries and the proximal clusters of Te vacancies serve as structural defects that are effective in promoting phonon scattering, thereby contributing to the overall thermoelectric performance enhancements.

The aforementioned applications utilizing HAADF imaging to characterize substitutional dopants, vacancies, and interstitial atoms are indeed confined to elements boasting higher atomic numbers. This limitation stems from HAADF imaging's inherent insensitivity to lighter elements, a characteristic dictated by its operational principles. Atoms with lower atomic numbers, like oxygen, typically remain indiscernible in most instances. Consequently, relevant research should incorporate characterization techniques capable of capturing real-space information on light elements simultaneously, such as negative spherical aberration high-resolution transmission electron microscopy (–Cs HRTEM, also known as NCSI), ABF imaging, integrated differential phase contrast (iDPC) techniques, etc. NCSI constructively superimposes linear and nonlinear contrast contributions to produce high-intensity maxima at the atomic column positions. This allows elements with low nuclear charges to be imaged at atomic resolution even when they are located in close proximity to strongly scattering heavy atoms.[14,15] Compared to the HAADF mode, which also uses an annular detector, ABF collects lower-angle scattered electrons with its annular detector, making it more sensitive to lighter elements. The iDPC utilizes a multi-segmented detector to collect information about the displacement of the centroid of a convergent beam diffraction pattern. Optimized algorithms integrate this information to determine the projected potential distribution within the sample, from which atomic position information can be inferred.[16,17] These characterization methods generally entail more intricate contrast influencing factors compared to HAADF imaging. Nevertheless, we can employ their contrast, which correlates positively with atom counts in atom columns, to depict the distribution of vacancies among light elements. For instance, benefiting from exceptionally low contrast delocalization, NCSI ensures that the imaging contrast of atomic columns remains unperturbed by scattering from adjacent columns.[18] This feature enables a distinct visualization of the vacancy distribution within oxygen columns, even when they are in close proximity to titanium columns near twin boundaries in BTO thin films. The research reveals that the formation of nanotwin lamellae during film deposition process acts as a structural optimization strategy for the system to cope with oxygen-deficient conditions. Notably, by estimating the mass-thickness distribution function derived from the contrast at neighboring $A/B$ sites around each oxygen column, and applying this as a corrective factor for oxygen contrast, one can effectively mitigate the impact of non-uniform sample thickness on oxygen contrast, which is a prerequisite for quantitative analysis of oxygen vacancies.

Another vital application of contrast information involves the statistical examination of chemical ordering. The methodology entails computing the correlation coefficient between the contrast at specific sublattice sites and a predefined template matrix, i.e., determining the degree of resemblance between the local contrast distribution and this template. Therefore, by judiciously selecting diverse template matrices, one can compute the extent of chemical ordering from various perspectives. The calculation method for the Pearson correlation coefficient is as follows:

$$r = \frac{\sum_m \sum_n \left(A_{mn} - \bar{A}\right)\left(B_{mn} - \bar{B}\right)}{\sqrt{\left(\sum_m \sum_n \left(A_{mn} - \bar{A}\right)^2\right)\left(\sum_m \sum_n \left(B_{mn} - \bar{B}\right)^2\right)}}.$$

That is, the ratio of the covariance to the variance, where $r$ is the Pearson correlation coefficient, $\boldsymbol{A}$ and $\boldsymbol{B}$ represent the locally normalized contrast matrix and the template matrix, respectively. For example, in the $\langle 1\text{–}10 \rangle$ oriented HAADF atomic image of PMN-PT,[19] the $B$-site sublattice simultaneously contains three types of atoms: Mg, Nb, and Ti. Among these, Nb, with its higher atomic number, presents a stronger contrast, whereas Mg and Ti exhibit relatively weaker contrasts. When adopting a $3 \times 3$ template matrix featuring alternating rows and columns of '1's and '0's, the correlation coefficient becomes a quantifiable measure describing whether Mg and Nb atoms exhibit an alternating pattern in the observed plane, suggestive of a doubled perovskite lattice arrangement, and consequently mirrors the chemical ordering of the $B$ sublattice. As the Ti content escalates, the degree of chemical ordering in PMN-PT decreases, corresponding to a decline in superlattice reflection intensity as the composition approaches the morphotropic phase boundary.

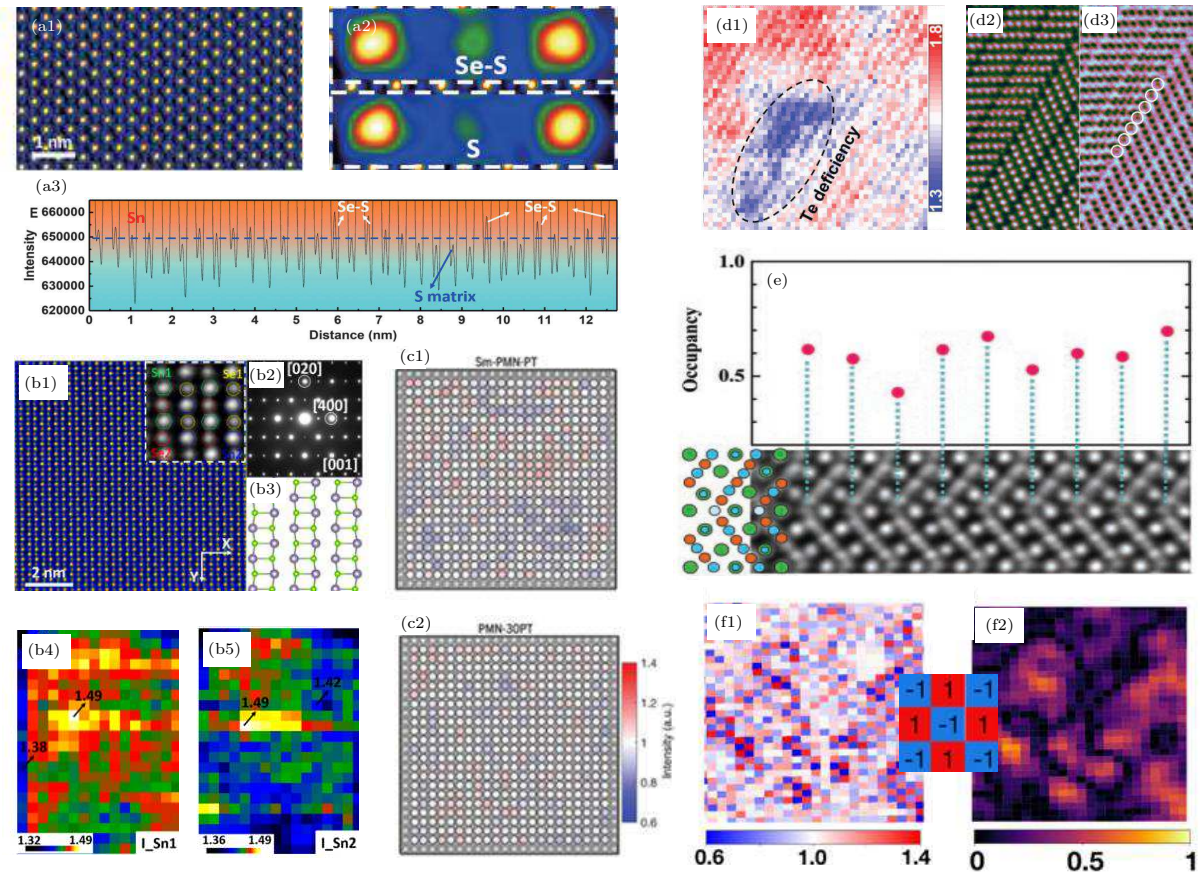



**Fig. 2.** Contrast quantitative analysis. (a) Contrast analysis in Se-doped SnS thermoelectric semiconductor crystals. (a1) Atomic HAADF image along the [001] zone axis. (a2) Enlarged image of (a1), showing the intensity variance between Se-substituted S and the SnS matrix. (a3) Intensity profile showing the higher intensity of Se-substituted S, compared with the SnS matrix. Reproduced with permission.[10] Copyright 2019, American Association for the Advancement of Science. (b) Contrast analysis in Te-alloyed SnSe crystals. (b1) Atomic HAADF image along the [001] zone axis, with enlarged image inset; four types of atom columns are marked as Sn1, Sn2, Se1 and Se2. (b2)–(b3) Electron diffraction pattern and structural model along the [001] zone axis. (b4)–(b5) Intensity map of Sn1 and Sn2 atom columns. Reproduced with permission.[11] Copyright 2018, American Chemical Society. (c) Normalized intensity distribution of the *A* sublattice for Sm-PMN-PT and PMN-30PT relaxor ferroelectric crystals in atomic HAADF image recorded along the [010] direction. Reproduced with permission.[12] Copyright 2019, American Association for the Advancement of Science. (d) Contrast analysis in $Sb_2Te_3$-based thermoelectric alloys. (d1) Intensity map showing a cluster of Te deficiency around a twin boundary. (d2)–(d3) Enlarged HAADF and ABF images showing Bi/Sb interstitial atoms at the twin boundary. Reproduced with permission.[13] Copyright 2022, Wiley-VCH. (e) Oxygen occupancy calculation at twin boundaries in BTO thin films using NCSI technique. The occupancy values derived from the measured intensities are shown as filled red circles. Reproduced with permission.[18] Copyright 2004, American Association for the Advancement of Science. (f) Schematic of correlation analysis to locate chemical ordered domains in PMN-PT crystals. (f1) Normalized Mg/Nb intensity map in ⟨1–10⟩ direction, (f2) Correlation coefficient (chemical ordering metric) map after computing with correlation kernel/template matrix, showing in the middle of (f1) and (f2). Reproduced with permission.[19] Copyright 2021, Springer Nature.

### 2.2. Lattice and strain analysis

The investigation of lattice information, which characterizes the three-dimensional periodic arrangement of atoms, is pivotal in deepening our comprehension of natural phenomena, elucidating the properties of substances, and directing the design and synthesis of novel materials. Compared to conventional lattice structure analysis methods such as x-ray diffraction (XRD), the atomic-level lattice presented under STEM provides a markedly more immediate and finely detailed perspective. Through the examination of lattice information encompassing lattice/sublattice constants/angles, bond lengths/angles, along with other specific spacings, and by probing their interrelations with pertinent physical properties, one can forge a link that explicates macroscopic behavior through microscopic structure. For example, in insulating materials, thermal conductivity is predominantly governed by atomic vibrations within the lattice, which are associated with factors such as lattice complexity, molecular weight, chemical bonding, and anharmonicity. In the BiSe$X$ ($X$ = Br, I) system,[20] characterized by its one-dimensional chain-like crystal structure, an extraordinarily low thermal conductivity ($\sim 0.27$ W·m$^{-1}$·K$^{-1}$ at 573 K) has been achieved. Via bond length analysis, it was ascertained that bismuth and halogen atoms exhibit considerable off-center displacements. The presence of elongated and feeble chemical bonds renders the system akin to a loosely packed, quasi-0D crystal structure, which significantly suppresses phonon transport. The pronounced temperature dependence of chemical bonds was also discussed through *in-situ* heating experiments. It was anticipated that, following enhancements to its electrical transport properties, this system could demonstrate substantial poten-

tial for application within the realm of thermoelectrics. In the case of relaxor ferroelectric materials (PMN-PT),[12] a remarkable piezoelectric coefficient $d_{33}$ (3400–4100 pC/N) has been achieved by innovatively introducing local structural heterogeneity through doping within the lattice. This approach synergistically combines with the traditional strategy of designing morphotropic phase boundaries, which serves to preserve low energy barriers between phases. The statistical analysis of sublattice distributions and $c/a$ ratio furnishes crucial evidence supporting the existence of local structural heterogeneities. Specifically, the large deviations evident in Sm-doped PMN-PT suggest the presence of localized, tetragonal-like regions, in stark contrast to the smaller deviations observed in PMN-30PT, which exhibits a phase closer to pure rhombohedral symmetry.

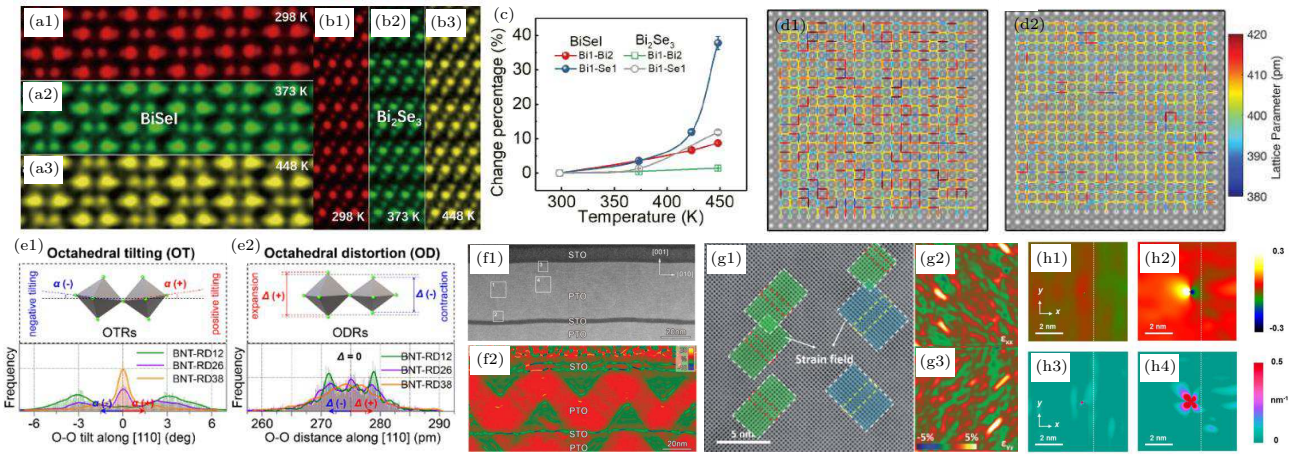



**Fig. 3.** Atomic lattice and local strain quantitative analysis. (a)–(c) Bond length analysis of 1D chain-like BiSeI and quintuple-layer $Bi_2Se_3$ crystals. HAADF images of (a1)–(a3) BiSeI and (b1)–(b3) $Bi_2Se_3$ acquired during *in-situ* heating at 298 K, 373 K and 448 K. (c) Temperature-dependent Bi–Bi and Bi–Se bond length changes in BiSeI and $Bi_2Se_3$ with respect to those at 298 K. Reproduced with permission.[20] Copyright 2020, Science China Press and Springer Nature. (d) Atomic distances between *A* sublattice positions in Sm–PMN-PT and PMN-30PT relaxor ferroelectric crystals along the [010] direction. Reproduced with permission.[12] Copyright 2019, American Association for the Advancement of Science. (e) Schematic illustration and statistical distribution of local structural orderings in the BNT-based system, including (e1) oxygen octahedral tilting (OT) and (e2) oxygen octahedral distortion (OD). Reproduced with permission.[21] Copyright 2022, Springer Nature. (f) Low magnification HAADF image and GPA analysis (OOP strain) of the upper PTO layer in an STO/PTO/STO/PTO/GSO multilayer. The *c* domains (red) exhibit a sinusoidal array, while the *a* domains (green) form triangular head-to-head configurations. Reproduced with permission.[22] Copyright 2015, American Association for the Advancement of Science. (g) ABF image and GPA analysis of PbSe-based thermoelectric semiconductors showing several nanostructures combining interstitial atoms. Reproduced with permission.[23] Copyright 2021, The Royal Society of Chemistry. (h) GPA analysis of deep cracks in STO thin film: (h1) OOP strain map, (h2) IP strain map, absolute values of (h3) $\mathrm{d}\varepsilon_{xx}/\mathrm{d}x$ and (h4) $\mathrm{d}\varepsilon_{yy}/\mathrm{d}y$. Reproduced with permission.[24] Copyright 2020, American Chemical Society.

The introduction of local disorder disrupts long-range correlations and average symmetry in materials, offering a wealth of degrees of freedom for property manipulation. Compared to leveraging sublattice information based on $A/B$-site cation arrangements, the computation of structural ordering, namely, octahedral tilting (OT) and distortion (OD) statistics, provides a more nuanced perspective for delineating local structural heterogeneities in perovskite systems. The computational principle for calculating structural ordering is similar to the method we discussed in Subsection 2.1 for computing chemical ordering using correlation coefficients. The difference lies in the fact that the basic information in the input matrix changes from contrast to lattice. In BNT-based relaxor ferroelectrics,[21] both OT and OD decrease as the doping concentration ascends. A diminution in anti-phase OT signifies a decrease in rhombohedral symmetry ($R3c$) proportion, alongside a decline in ferroelectric stability, manifesting as a lower $T_d$. Point-to-point correlation analysis reveals that in low-doping systems, polarization facilitated by *B*–O displacement promotes the formation of anti-phase OT. Moreover, a positive correlation is evident between anti-phase OT and polarization deviation. However, as the doping concentration increases, the correlations between anti-phase OT and *B*–O displacement, as well as polarization deviation, progressively diminish. With the amplification of multi-directional displacements of *A*-site cations, the disparity in *A*–O bond lengths is augmented, enabling them to supplant anti-phase OT as the predominant mechanism driving polarization deviations in high-doping systems. The coupling between local order and polarization evolution constitutes a pivotal microstructural foundation, instrumental in elucidating the genesis of substantial dynamic electromechanical responses.

While atomic coordinates precisely extracted from atomic-resolution STEM images directly allow for local strain calculation, geometric phase analysis (GPA) remains a highly accurate and universally applicable method for mapping strain fields. GPA involves performing a Fourier transform on the real-space STEM image, with its reciprocal space information

characterized by a two-dimensional Bragg reflection pattern along specified axes. By designating small apertures around two non-collinear diffraction spots and applying the inverse Fourier transform, the phase components of the resulting images reveal information about the two-dimensional local displacement field of atomic planes:

$$P_{\mathrm{g}}(\boldsymbol{r}) = -2\pi \boldsymbol{g}\boldsymbol{u}(\boldsymbol{r}), \;\; u_i = -\frac{P_i}{2\pi} d_i.$$

Here, $P_{\mathrm{g}}(\boldsymbol{r})$ represents the geometric phase of a set of lattice fringes with reciprocal lattice vector $\boldsymbol{g}$, $\boldsymbol{u}(\boldsymbol{r})$ represents the displacement, $\boldsymbol{r}$ is the position coordinate in the image, $d$ is the fringe spacing (equal to $1/g$). Strain map can then be quantitatively derived through the derivative of this displacement field:[25]

$$\varepsilon_{ij} = \frac{1}{2}\left(\frac{\partial u_i}{\partial x_j} + \frac{\partial u_j}{\partial x_i}\right), \;\; \Delta_{ij} = \frac{1}{2}\left(\frac{\partial u_i}{\partial x_i} + \frac{\partial u_j}{\partial x_j}\right),$$

$$\omega_{ij} = \frac{1}{2}\left(\frac{\partial u_j}{\partial x_i} - \frac{\partial u_i}{\partial x_j}\right).$$

As a semi-quantitative lattice image processing technique that reveals the spatial distribution of relative elastic strains, GPA is extensively employed in measuring strain and strain gradient fields near characteristic features in electronic functional materials, encompassing domains, grain boundaries, precipitates, dislocations, and microcracks. For instance, in ferroelectric PTO thin films,[22] the spatial arrangement of topological domain structure is characterized by the fluctuations of out-of-plane strain, thereby distinguishing between out-of-plane and in-plane polarized domains. In PbSe-based thermoelectric semiconductors,[23] distinctive structural defects, such as interstitial clusters, which are prevalent in systems exhibiting low lattice thermal conductivity, can be precisely identified. These defects give rise to pronounced lattice distortions in the matrix, thereby promoting phonon scattering. In the characterization of piezoelectric STO thin film cracks,[24] comparative studies of strain, strain gradient, and polarization distributions near the crack tip have unveiled that strain gradient is the predominant driver behind the formation of substantial polarization in this region, a phenomenon known as flexoelectric polarization.

### 2.3. Atomic displacement and polarization analysis

Polarization, serving as the pivotal order parameter of ferroelectricity, quantifies the degree of displacement between positive and negative charge centers in dielectrics. Considering the predominantly positive correlation between atomic displacements and polarization — mediated by the Born effective charge (ignoring nondiagonal terms),[26] yet oppositely directed — the polarization distribution can be characterized by quantitative computations of atomic displacements. The Born effective charge could be calculated by

$$Z^*_{i,\alpha\beta} = \frac{V}{e}\frac{\partial P_\alpha}{\partial x_{i,\beta}}. \tag{1}$$

Here, $\boldsymbol{Z}$ represents the Born effective charge, $V$ is the unit cell volume, $e$ is the electron charge, $\boldsymbol{P}$ represents the polarization and $x$ the atomic displacement. For a system, each element has a corresponding fixed Born effective charge. Hereafter, unless specifically noted, discussions will treat atomic displacement statistics and polarization calculations interchangeably, making no explicit differentiation. Notably, the displacement that represents the magnitude of polarization is not limited to a single type. For example, in perovskite systems, the off-center displacements of $A/B$ ions can be used to calculate the polarization, even though they are both cations. This typically occurs in imaging modes that do not consider oxygen atoms (such as HAADF), where the positions of $B$ ions are used to some extent as a proxy for the centers of the associated oxygen octahedra.

Ferroelectric materials exhibit a propensity to form distinct domains, each identified by differing polarization directions, demarcated by boundaries known as domain walls. This arrangement minimizes uncompensated depolarizing fields at surfaces, accommodates elastic strains, and ultimately minimizes the total free energy of the system. Functional domain walls constitute a vibrant area of research in the realm of piezoelectrics and ferroelectrics, concentrating primarily on elucidating the precise mechanisms of domain wall conductivity, electrically manipulating domain wall density and geometries to fabricate high-density non-volatile memory and logic devices, exploring the anomalous photovoltaic effect, stabilizing negative capacitance, harnessing GHz-frequency resonant domain wall motion (vibrations within domain wall-rich samples) for ultra-low loss thin-film devices, dynamically modulating thermal properties through controlled domain wall density via epitaxial strain and film thickness adjustments, achieving magnetoelectric coupling, etc.[27] Real-time tracking of domain wall motion under an external field and detecting its atomic-scale polarization rotation, known as the *in-situ* biasing technique, is a critical innovative technology at the intersection of domain wall engineering and electron microscopy analysis.[28] In conclusion, atomic-scale characterization and associated quantitative analyses of domain walls constitute a vital component of research in both piezoelectrics and ferroelectrics.

Domain walls essentially represent regions of maximum variation in polarization. Hence, their localization is primarily accomplished through quantifying polarization deviations and implementing threshold-based segmentation.[19] Specifically, the procedure initiates with determining the deviation angle of

each polarization vector from the average of polarization vectors within its immediate lattice neighborhood:

$$\theta_{\mathrm{DP}} = \frac{\sum_i |\theta_i - \theta_0|}{N}. \tag{2}$$

Here, $\theta_{\mathrm{DP}}$ represents the deviation angle, $\theta_0$ is the polarization angle of the central unit cell, $\theta_i$ is the polarization angle of the unit cells surrounding the central one, and $N$ the neighboring number. Subsequently, a Sato filter is employed, setting a median threshold as a binary segmentation criterion, thereby distinguishing regions with notably larger polarization deviations, indicative of domain walls, from those with minor deviations suggestive of smooth transition areas. For instance, in BNT-based relaxor ferroelectrics,[21] observations reveal not only the connection between domain walls and smoothly transitioning polarization zones, but also a concentration-dependent dynamic response: as doping concentration increases, dispersed, minor domain wall regions progressively coalesce into larger aggregates. The characterization of local polarization deviations elucidates the morphology, dimensions, and dispersion patterns of the polar nanoregions (PNRs) in the BNT-based relaxor system. Statistical analysis of domain wall angles, defined by the peak polarization deviation between each domain wall and its adjacent units, permits distinction of domain wall types and investigation of the evolution of domain structures. In PMN,[19] domain wall angles predominantly cluster between 10° and 35°, reflecting its characteristic relaxor 'slush' polar state. As the Ti content increases, the domain wall angle distribution tends to shift towards higher values, presaging the emergence of long-range polarization and onset of ferroelectric behavior.

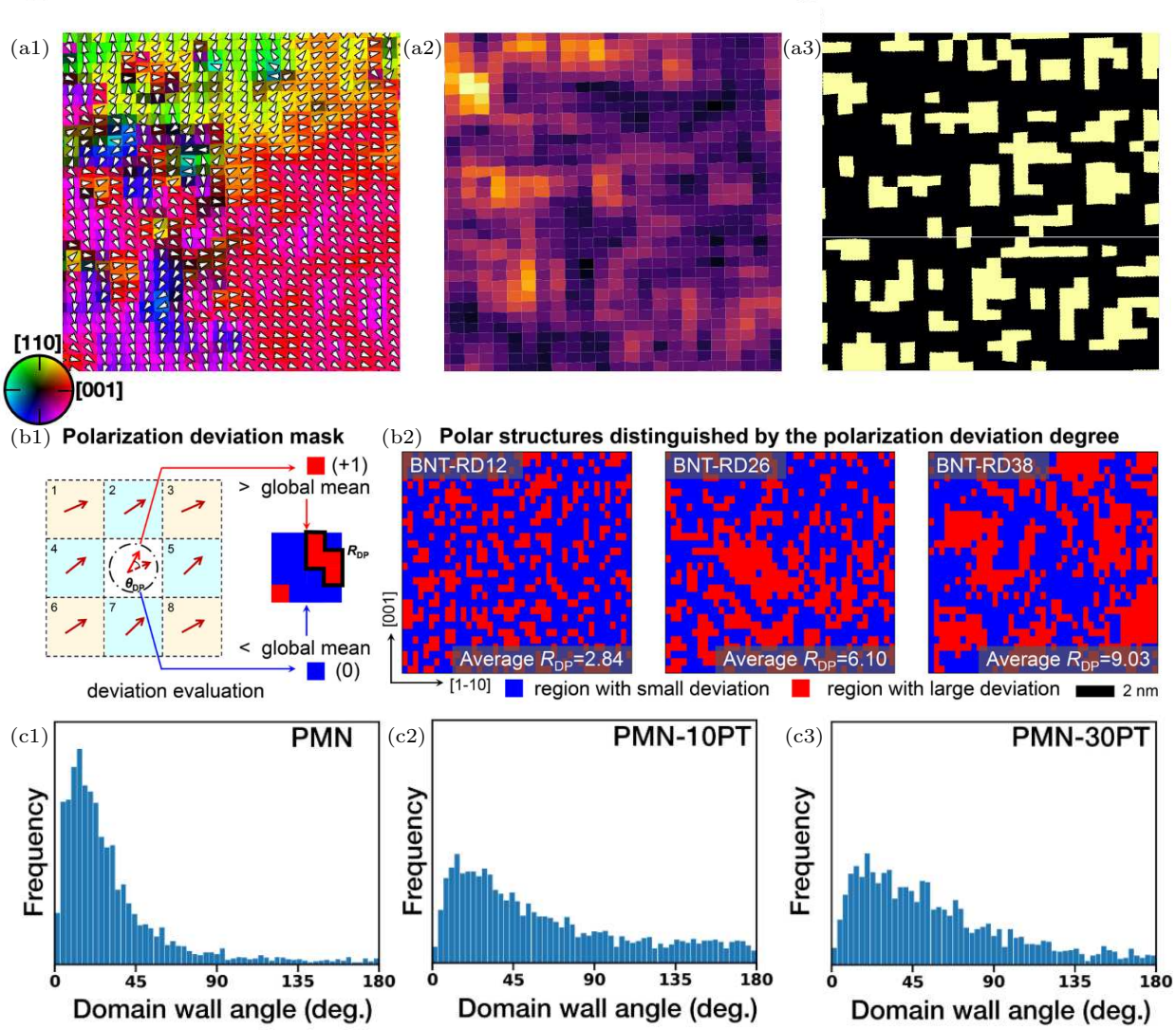



**Fig. 4.** Polarization quantitative analysis and ferroelectric domain structure characterization. (a) Domain wall identification methods in perovskites (e.g., PMN-PT). (a1) Polarization vector map in PMN. (a2) Standard deviation of polarization. (a3) Local maxima map determined through threshold-based segmentation using Sato filter. The local maxima corresponding to domain walls are highlighted as yellow blocks. Reproduced with permission.[19] Copyright 2021, Springer Nature. (b) Evaluation of the deviation degree of polarization in relaxor ferroelectric BNT-based system. (b1) Schematic illustration of the method. (b2) Statistic map showing relevance between the distribution of polarization deviation degree and material composition. Reproduced with permission.[21] Copyright 2022, Springer Nature. (c) Domain wall angle distribution in PMN-PT system. Reproduced with permission.[19] Copyright 2021, Springer Nature.

Atomic displacements can be presented in error bar plots to study the differences in polarization states between domains and the evolution of polarization near domain walls, particularly for matrix systems with large domains and long-range domain walls. Specifically, the $X$-axis of these plots generally represents the unit cell sequence or distance, and this statistical analysis is conducted perpendicular to the domain wall, meaning that a column of unit cells parallel to the domain wall would be included in the same error bar.[29–31] This approach describes the relationship between polarization and the distance from the domain wall through the overall trend of the curve, while the local error bars indicate the uniformity of polarization within the field of view. It could also be used to analyze sublattice spacing and the $c/a$ ratio, which may exhibit coupling with polarization.[29,30]

In addition to the development of polarization analysis techniques themselves, updates in other characterization techniques combined with polarization analysis can lead to new discoveries. For example, the development of real-time spatial imaging techniques has made it possible to simultaneously image the four-dimensional distribution of interfacial charge and ferroelectric polarization. Researchers have observed accumulation charges at the interface in $SrTiO_3$/$BiFeO_3$ heterojunctions caused by polarization fields.[32]

Compared to contrast and lattice information, polarization and domain-related analysis in piezoelectric/ferroelectric materials offer broader application prospects. Microscopic polarization and domain state distributions, as observed under the electron microscope, provide a theoretical basis for understanding macroscopic material properties, with a focus on structure–property relationships. Additionally, polarization analysis can characterize unique polarization states, enabling their development as functional elements in microelectronic devices, emphasizing the discovery and controlled synthesis of novel structures. We will outline representative works in both areas, highlighting the critical role of polarization-related quantitative analysis in the field of piezoelectric/ferroelectric materials.

#### 2.3.1. Enhanced performances: Polarization in piezoelectric relaxors

The pursuit of advanced performance and the exploration of intrinsic structural mechanism remain enduring themes in materials science. Piezoelectric ceramics, capable of converting mechanical energy to electricity and vice versa, have seen extensive implementation in industrial applications, such as sensors and actuators. In perovskite ferroelectrics, piezoelectric performance is typically quantified by the piezoelectric coefficient, denoted as

$$d = 2P_s Q\varepsilon, \tag{3}$$

where $d$ is the piezoelectric coefficient, $P_s$ represents the spontaneous polarization, $Q$ is the electrostrictive coefficient, and $\varepsilon$ is the dielectric permittivity. The tunability of $\varepsilon$ leads to a correlated enhancement of the piezoelectric coefficient with the dielectric constant. $\varepsilon$ shows a positive association with the curvature (i.e., the second derivative $\partial^2 G/\partial P^2$) of the polarization-free energy density curve. A diminished curvature, indicating a flatter free energy landscape, results in an elevated dielectric constant, subsequently boosting piezoelectric response. Key strategies currently employed to flatten the thermodynamic energy landscape entail controlling chemical composition for designing morphotropic phase boundaries (MPB), introducing nanoscale local structural heterogeneities to manipulate interfacial energetics, incorporating charged domain walls to generate depolarizing fields, leveraging external mechanical stresses, etc.

The mapping of polarization vectors in high-resolution atomic images has opened avenues for investigating diverse microstructural mechanisms underlying different high-performance piezoelectric materials.[33] For instance, in lead-free piezoelectric BFO thin films,[34] epitaxial constraints inducing an MPB enable a reversible transformation between tetragonal-like and rhombohedral-like phases under electric field application. Specifically, T-phase and R-phase are distinguished by their lattice constants and polarization orientations. As depicted, a T-phase is interspersed between dual R-phases, with a smooth transition occurring over roughly ten unit-cells, accompanied by variations in the $c/a$ ratio, and without the presence of misfit dislocations. This structural trait can be regarded as indicative of a long-range ordered matrix, devoid of local disorder. When short-range ordered PNRs are introduced into the long-range ordered matrix, they can rotate facilely and respond quickly under external electric fields and stress stimuli. This mechanism eases the necessary energy barrier for dipole rotation, thereby enhancing the piezoelectric response. For example, in the endeavor to improve the piezoelectric performance of the PMN-PT relaxor ferroelectric system by manipulating the interface energy via local structural heterogeneity,[35] polarization analysis was pivotal in evidencing the existence of PNRs. Specifically, the tetragonal matrix, characterized by polarization along the [010] axis, was found to incorporate minor orthorhombic-like nanoregions, exhibiting polarization along the [110] axis. Furthermore, when the long-range ordered matrix disappears and the system is predominantly filled with short-range ordered PNRs, it evolves into a state replete with an abundance of low-angle domain walls, maintaining a multi-domain polarization state with low energy, which is known as the relaxor 'slush' polar state. The relaxation behavior of the system manifests in frequency dispersion occurring during phase transitions between

various ferroelectric phases. The augmentation of its piezoelectric properties, however, is attributable to the synergistic effects of multiple contributing factors. Firstly, the characteristics of the aforementioned PNRs find their fullest expression within the relaxor 'slush' polar state. Secondly, considering the multiphase coexistence, O-phase presents 12 possible ⟨110⟩-oriented spontaneous polarization directions, whereas R-phase has 8 along ⟨111⟩, and T-phase only 6 along ⟨001⟩. Polarization vectors of the O-phase, to some extent, bridge those of the R and T phases, significantly reducing the energy barriers required for polarization rotation. Lastly, the high-density low-angle domain walls, functioning as conduits between PNRs, markedly diminish the polarization anisotropy. The design strategy of boosting the piezoelectric performance of materials (peak values of the piezoelectric coefficient $d_{33}$ or inverse piezoelectric coefficient $d^*_{33}$, broad compositional stability, etc.) by introducing the relaxor 'slush' polar state has proven successful in perovskites such as KNN[36,37] and BTO.[38]

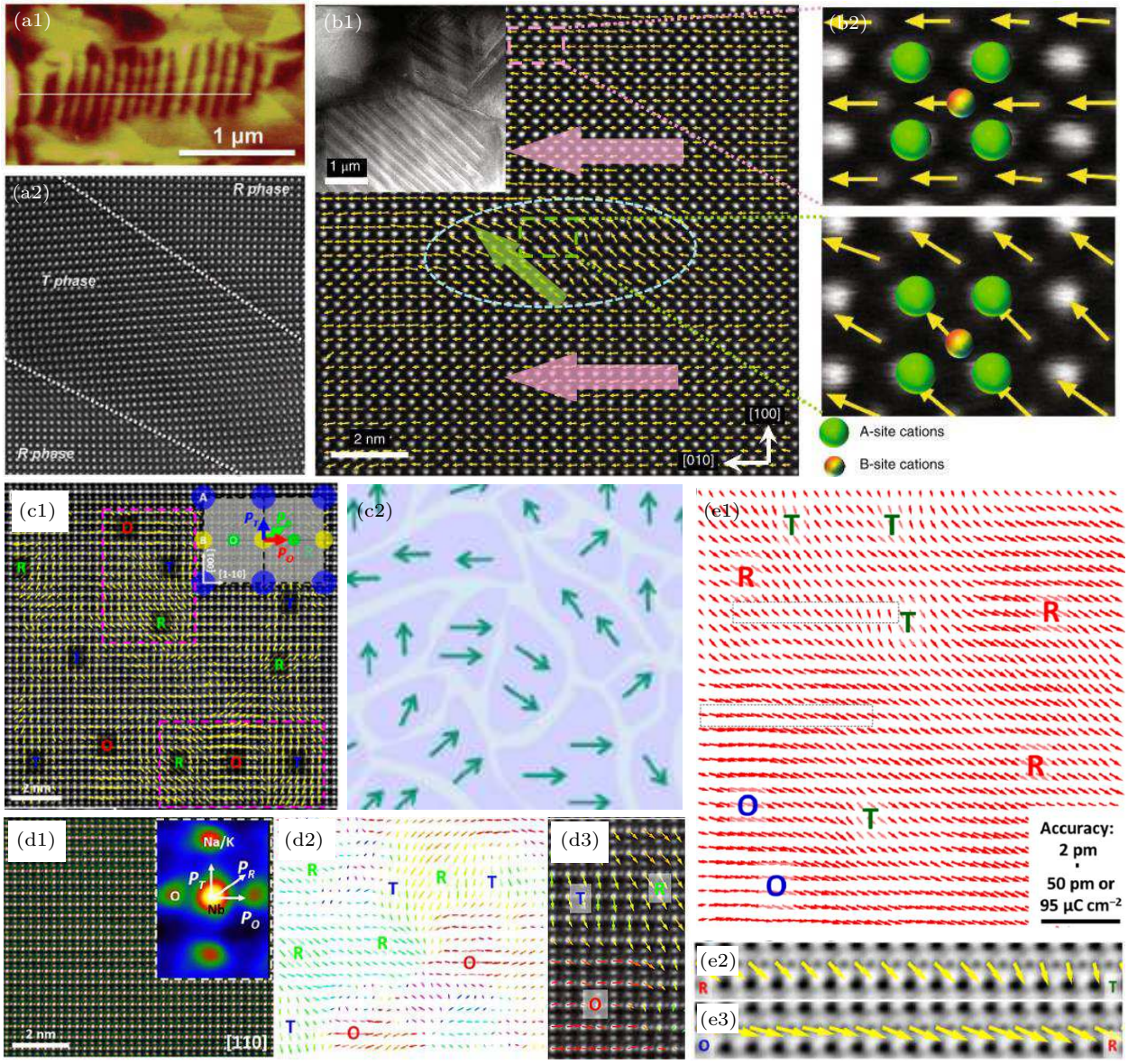



**Fig. 5.** Polarization quantitative analysis in relaxors with enhanced piezoelectric response. (a) Long-range ordered matrix without local disorder in piezoelectric BFO thin films. (a1) High-resolution AFM image of a mixed phase region. (a2) HRTEM image of the boundaries between R and T phases. Reproduced with permission.[34] Copyright 2009, American Association for the Advancement of Science. (b) Long-range ordered matrix with short-range ordered PNRs in PMN-PT relaxor ferroelectric system. (b1) Dark-field TEM (upper left corner) and TEM images at room temperature, recorded along the crystallographic [001] direction. The polar vectors (arrows) are given for each unit-cell column. (b2) Enlarged polarization maps of featured regions. Reproduced with permission.[35] Copyright 2018, Springer Nature. (c)–(e) 'Slush' polar states (i.e., the system is predominantly filled with short-range ordered PNRs) in (c)–(d) KNN and (e) BTO-based systems, with continuous polarization rotation and multiphase coexistence. Reproduced with permission.[36] Copyright 2019, American Chemical Society. Reproduced with permission.[37] Copyright 2021, American Chemical Society. Reproduced with permission.[38] Copyright 2018, American Chemical Society.

### 2.3.2. Exotic structures: Polarization of topological states

Topology, a branch originating in mathematics, primarily investigates spatial invariance under smooth and continuous deformations. In materials science, the incorporation of topological concepts facilitates the examination of exotic states in condensed matter physics, encompassing real-space topological structures and various reciprocal-space topological phenomena, exemplified by topological insulators. Among these, spin topological features in ferromagnets have garnered extensive attention, spurring analogous explorations into polar topological structures in ferroelectrics. In the early 21st century, employing the effective Hamiltonian method derived from first-principles, researchers first reported the realization of vortex-like polarization patterns in BTO quantum dots and nanowires.[39] Compared to bulk materials, low-dimensional ferroelectrics are distinguished by their substantial depolarizing fields, which suppress polarization magnitudes and mitigate anisotropy. Electric dipoles rearrange into flux-closure or vortex domains to optimize energy by minimizing depolarization effects. Despite a plethora of theoretical predictions emerged thereafter,[40] experimental verification of polarization topological structures stagnated for nearly a decade, hindered by technical obstacles and a dearth of sophisticated characterization tools. Progress in high-resolution characterization techniques and the advent of polarization quantification methods have enabled us not only to directly observe continuous polarization rotation near ferroelectric thin film interfaces, validating relevant theoretical propositions, but also to witness a series of exotic polar topological architectures. These include flux-closure domains, vortices, bubbles, spiral states, hedgehog states, polar skyrmions, polar merons, etc.[27] The emergence of a particular topological structure arises from the competition and synergistic effects among diverse energy terms, including elastic energy (i.e., strain energy, influenced by epitaxial constraints and domain formation), electrostatic energy (i.e., depolarization energy, related to built-in electric fields and bound charges), polarization or chemical gradient energy (i.e., energy required for polarization rotation or magnitude alteration), and interfacial coupling energy. Engineering such nonuniform polarization landscapes in ferroelectrics promises substantial potential performance benefits, including heightened electronic conductivity, augmented magnetization, giant electromechanical response, negative capacitance effects, chirality, etc. Furthermore, they offer considerable guidance for the blueprinting of nanoelectronic devices, including ultradense nonvolatile memory systems and low-power transistors.

Acquiring atomic-level details from STEM imagery and computing polarization vector maps enable the investigation of the distinctive features of polarization distribution across various ferroelectric topological structures. In PTO thin films,[22] for instance, periodic arrays of flux-closure domains, mediated by tensile strain from the substrate, have been documented. The figure showcases two archetypal, periodically recurring flux-closure domain structural units: counterclockwise quadrants formed by the combination of regions 1 and 2 stacked vertically, and clockwise quadrants stemming from regions 3 and 4. Each observation zone contains a 180° domain wall along with two 90° domain walls. The existence and periodicity of flux-closure domains are contingent upon film thickness, with an optimal range spanning from 15 nm to 36 nm. Thinner films tend to adopt full strain compliance without domain formation, whereas thicker films incline towards the emergence of alternating $a/c$ domain arrangements. In $PbTiO_3/SrTiO_3$ ferroelectric/paraelectric superlattices,[41] the competition among charge, orbital, and lattice degrees of freedom gives rise to a long-range ordered array of nanoscale vortices/antivortices with alternating rotational directions. The lateral periodicity of this structure is approximately commensurate with its superlattice period, roughly estimated at approximately 10 nm. Polarization analyses disclose a continuous rotation of polarization vectors around a central point within the vortices, devoid of discernible domain walls. This starkly contrasts with conventional ferroelectric domains or flux-closure quadrants, which feature uniform domains interconnected via distinct domain walls. The existence of vortex arrays is intricately linked to the superlattice periodicity, exhibiting an optimal range falling within 10–18 nm. At overly tight periodicities, the system favors in-plane polarization components ($a_1/a_2$ domains) only, sacrificing elastic energy to minimize electrostatic and gradient energies. Conversely, with more spacious periods, flux-closure formations arise, featuring discrete domains enveloping local polarization gradients at domain boundaries. In $PbTiO_3/SrTiO_3$ superlattices,[42] the existence of polar skyrmions has been detected at ambient temperature by tuning epitaxial constraints. Planar-view HAADF images visualized the atomic displacement distribution encircling individual polar skyrmions, specifically revealing a convergent pattern of reversed Ti displacements streaming inward from the skyrmion's periphery towards its core, mirroring a hedgehog-like configuration. Cross-sectional HAADF images disclosed cylindrical polar regions exhibiting anti-parallel (up-down) polarization states, accompanied by polarization vector rotations near the $PbTiO_3/SrTiO_3$ interface. Through 4D-STEM analysis, which integrates ADF signal with the in-plane probability current flow derived from the first moment of the diffracted beams, Bloch-like characteristics were observed, wherein the probability current flow encapsulated the polar order from the skyrmion bubble's epicenter and its upper hemisphere. Corresponding simulations further validated this observation. Synthesizing the aforementioned findings, the polar skyrmions manifest a hybrid nature, embodying both a hedgehog-like structure and a Bloch-type, in-plane compo-

nent. Subsequently, within a year, polar merons were detected in ultrathin $PbTiO_3$ films through the manipulation of epitaxial strain imparted via a $SmScO_3$ substrate.[43] Polar merons represent a non-coplanar topological construct, characterized by an out-of-plane polarization at the nucleus and an in-plane polarization in the peripheral region. As half-skyrmions carrying a topological charge of $1/2$, merons can adopt either a hedgehog- or vortex-type distribution schema. This investigation accomplished the characterization of merons through high-resolution STEM imaging coupled with polarization vector mapping, meticulously inspecting both cross-sectional and planar views. Specifically, in the cross-sectional orientation, domains alternate between trapezoidal and inverted trapezoidal geometries, corresponding to $a/c$ domain configurations and featuring in-plane (IP) versus out-of-plane (OOP) polarization, respectively. From the planar perspective, a stripy polarization configuration emerges from the alternating alignment of head-to-head and tail-to-tail domain walls, with a stripe spacing of approximately 8 nm. Each domain wall accommodates merons, thus assembling into meron arrays. Similarly, the average interval of around 8 nm between adjacent merons along a single domain wall suggests a lattice-like disposition of merons in the plane. Head-to-head domain walls host merons arranged in a convergent pattern, whereas on tail-to-tail domain walls, they display a divergent arrangement. Convergent-type merons feature a reduced in-plane polarization component at their cores, implying a potentially substantial out-of-plane polarization component. Furthermore, the presence of antimerons, situated amidst contiguous merons in each meron array, has also been confirmed. In addition to discovering new topological structures and developing more precise and controllable methods for preparing topological states, broadening the dimensions of polarization characterization to reveal three-dimensional topological orderings in ferroelectric nanostructures beyond films (e.g., nanoparticles, decoupled from the positive influence of epitaxial strain) through atomic electron tomography and reconstruction also holds significant prospects for future development.[44]

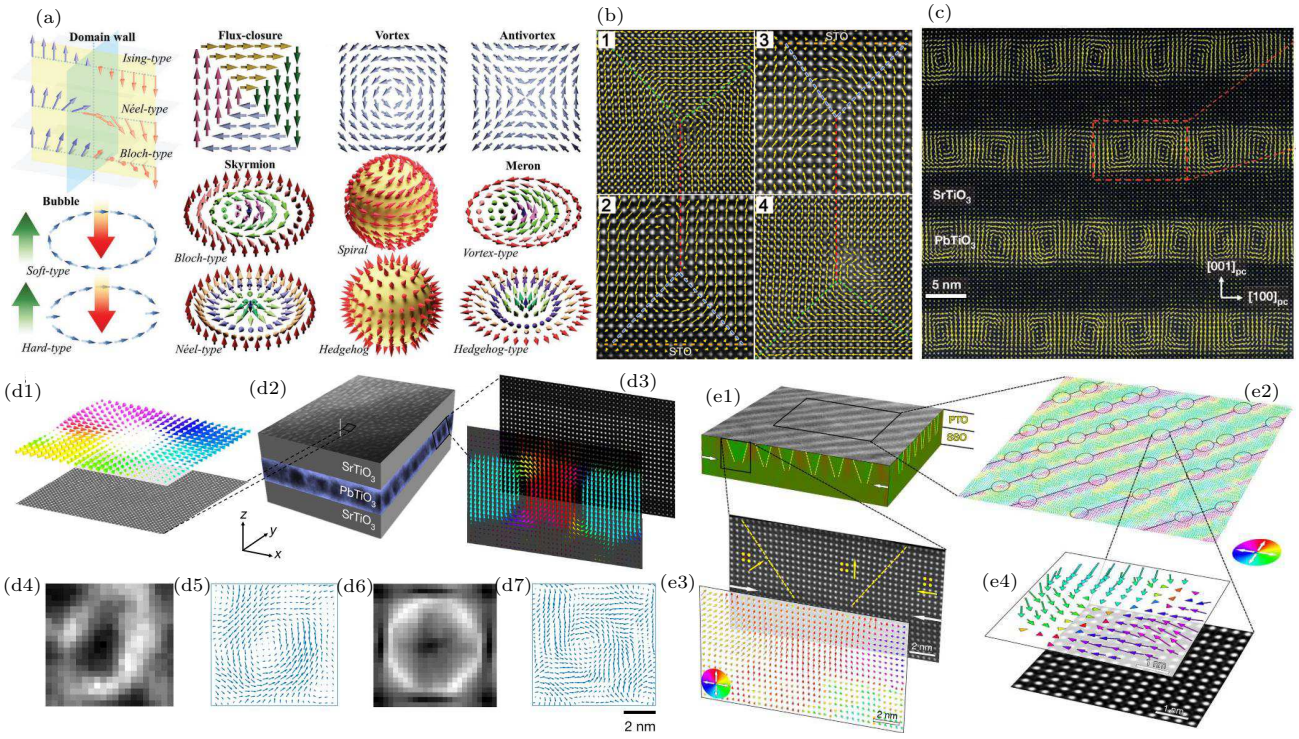



**Fig. 6.** Polarization quantitative analysis of exotic topological states. (a) Schematics of typical topological structures in ferroics. Order parameters, such as polarization and magnetization, represented as arrows. Reproduced with permission.[27] Copyright 2020, Wiley-VCH. (b) Superposition of HAADF images and Ti displacement vector maps showing the flux-closure quadrants in PTO thin films. Reproduced with permission.[22] Copyright 2015, American Association for the Advancement of Science. (c) Cross-sectional HR-STEM image with an overlay of the polar displacement vectors for a $SrTiO_3/PbTiO_3$ superlattice, showing presence of an array of vortex–antivortex pairs in each PTO layer. Reproduced with permission.[41] Copyright 2016, Springer Nature. (d) Observation of polar skyrmion structure in $PbTiO_3/SrTiO_3$ superlattice. (d1) Ti-displacement vector map (top) based on planar view HAADF image (bottom) of a single skyrmion bubble, showing the hedgehog-like skyrmion architecture. (d2) The sketch of the superlattice. (d3) Ti-displacement vector map (front) based on cross-sectional image (back), showing a cylindrical domain with anti-parallel polarization. (d4)–(d5) The 4D-STEM image of superlattice gives (d4) the ADF image and (d5) maps of polar order using the probability current flow. (d6)–(d7) Multislice simulations of the beam propagation through the model structure, showing (d6) the ADF image and (d7) the probability current flow. Reproduced with permission.[42] Copyright 2019, Springer Nature. (e) Observation of polar meron structure in $PbTiO_3/SmScO_3$ thin film. (e1) A sketch of a planar-view HAADF image overlaid with a cross-sectional strain map, displaying an overview of the PTO film. (e2) Polarization map based on planar-view HAADF image of stripe domains, showing the convergent meron arrays at head-to-head domain walls. (e3) Polarization map (front) based on cross-sectional HAADF image (back), showing a trapezoidal domain with the convergent polarization configuration. (e4) Polarization map (top) of a magnified polar meron with the convergent polarization configuration based on planar-view HAADF image (bottom). Reproduced with permission.[43] Copyright 2020, Springer Nature.

## 3. Summary and prospects

The capability of AC-STEM to simultaneously acquire multiple atomic-resolution images and spectra significantly facilitates the characterization of electronic functional materials. In thermoelectric materials, atomic-scale defect engineering and substitutional doping strategies in alloys constitute crucial microstructural mechanisms for optimizing carrier and phonon transport properties, areas where strain and contrast analyses excel.[10,11] In piezoelectric/ferroelectric materials, lattice analysis can reveal the underlying local structural heterogeneities that facilitate substantial dynamic electromechanical responses.[12] Crucially, the quantification of local atomic displacements empowers the profiling of polarization (the order parameter of ferroelectrics), thereby catalyzing groundbreaking research aimed at deciphering polarization landscapes and domain architectures.[31,32,45–49] This encompasses studies on the foundation of functional domain boundaries or their dynamic redistribution under external fields,[19,21,30,31] the design of relaxor polar states with continuous rotation of electric dipoles and multiphase coexistence to enhance piezoelectric performance,[36–38] the exploration and manipulation of topological polar states to guide nanoelectronic device designs,[25,41–43] and the investigation into coupling relationships between various atomic-scale defects and localized polarization.[50–55] In tandem with advancements and innovations in electron microscopy hardware, quantitative analytical techniques are poised to evolve towards automation, batch handling, *in-situ* implementation,[28] multi-dimensionality,[44] and enhanced precision,[28] thereby perpetually reinforcing our capacity for in-depth investigations into the microcosm.

## Acknowledgments

Project supported by the financial support from the National Key R&D Program of China (Grant No. 2021YFB3201100), the National Natural Science Foundation of China (Grant No. 52172128), and the Top Young Talents Programme of Xi'an Jiaotong University.

## References

[1] Crewe A V, Wall J and Langmore J 1970 *Science* **168** 1338
[2] Pennycook S J and Jesson D E 1991 *Ultramicrosc* **37** 14
[3] Jones L, Yang H, Pennycook T J, Marshall M S J, Van Aert S, Browning N D, Castell M R and Nellist P D 2015 *Adv. Struct. Chem. Imaging.* **1** 8
[4] Galindo P L, Kret S, Sanchez A M, Laval J Y, Yáñez A, Pizarro J, Guerrero E, Ben T and Molina S I 2007 *Ultramicrosc* **107** 1186
[5] Bárcena-González G, Guerrero-Lebrero M P, Guerrero E, Yañez A, Fernández-Reyes D, González D and Galindo P L 2017 *Ultramicrosc* **182** 283
[6] Jones L and Nellist P D 2013 *Microsc. Microanal.* **19** 1050
[7] Jones L, Varambhia A, Beanland R, Kepaptsoglou D, Griffiths I, Ishizuka A, Azough F, Freer R, Ishizuka K, Cherns D, Ramasse Q M, Lozano-Perez S and Nellist P D 2018 *Microscopy* **67** 98
[8] https://www.hremresearch.com/Eng/download/documents/PPA%20Manual%20v5.0.pdf
[9] https://www.hremresearch.com/Eng/download/documents/SmartAlign%20Manual.pdf
[10] He W K, Wang D Y, Wu H J, *et al.* 2019 *Science* **365** 1418
[11] Qin B C, Wang D Y, He W K, Zhang Y, Wu H J, Pennycook S J and Zhao L D 2019 *J. Am. Chem. Soc.* **141** 1141
[12] Li F, Cabral M J, Xu B, Cheng Z X, Dickey E C, LeBeau J M, Wang J L, Luo J, Taylor S, Hackenberger W, Bellaiche L, Xu Z, Chen L Q, Shrout T R and Zhang S J 2019 *Science* **364** 264
[13] Qin H X, Qu W B, Zhang Y, Zhang Y S, Liu Z H, Zhang Q, Wu H J, Cai W and Sui J H 2022 *Adv. Sci.* **9** 2200432
[14] Jia C L, Lentzen M and Urban K 2003 *Science* **299** 870
[15] Jia C L, Lentzen M and Urban K 2004 *Microsc. Microanal.* **10** 174
[16] Lazić I, Bosch E G T and Lazar S 2016 *Ultramicrosc* **160** 265
[17] Lazić I and Bosch E G T 2017 *Adv. Imaging Electron Phys.* **199** 75
[18] Jia C L and Urban K 2004 *Science* **303** 2001
[19] Kumar A, Baker J N, Bowes P C, Cabral M J, Zhang S J, Dickey E C, Irving D L and LeBeau J M 2021 *Nat. Mater.* **20** 62
[20] Wang D Y, Huang Z W, Zhang Y, Hao L J, Wang G T, Deng S H, Wang H L, Chen J, He L H, Xiao B, Xu Y D, Pennycook S J, Wu H J and Zhao L D 2020 *Sci. China Mater.* **63** 1759
[21] Yin J, Shi X M, Tao H, Tan Z, Lv X, Ding X D, Sun J, Zhang Y, Zhang X M, Yao K, Zhu J G, Huang H B, Wu H J, Zhang S J and Wu J G 2022 *Nat. Commun.* **13** 6333
[22] Tang Y L, Zhu Y L, Ma X L, Borisevich A Y, Morozovska A N, Eliseev E A, Wang W Y, Wang Y J, Xu Y B, Zhang Z D and Pennycook S J 2015 *Science* **348** 547
[23] Xiao Y, Liu W, Zhang Y, Wang D Y, Shi H N, Wang S N, Jin Y, Qu W B, Wu H J, Ding X D, Sun J and Zhao L D 2021 *J. Mater. Chem. A* **9** 23011
[24] Wang H G, Jiang X J, Wang Y, Stark R W, van Aken P A, Mannhart J and Boschker H 2020 *Nano Lett.* **20** 88
[25] Hÿtch M J, Snoeck E and Kilaas R 1998 *Ultramicrosc* **74** 131
[26] Neaton J B, Ederer C, Waghmare U V, Spaldin N A and Rabe K M 2005 *Phys. Rev. B* **71** 014113
[27] Chen S Q, Yuan S, Hou Z P, Tang Y L, Zhang J P, Wang T, Li K, Zhao W W, Liu X J, Chen L, Martin L W and Chen Z H 2020 *Adv. Mater.* **33** 2000857
[28] Liu Z R, Wang H, Li M, Tao L L, Paudel T R, Yu H Y, Wang Y X, Hong S Y, Zhang M, Ren Z H, Xie Y W, Tsymbal E Y, Chen J S, Zhang Z and Tian H 2023 *Nature* **613** 656
[29] Jia C L, Nagarajan V, He J Q, Houben L, Zhao T, Ramesh R, Urban K and Waser R 2007 *Nat. Mater.* **6** 64
[30] Seidel J, Martin L W, He Q, Zhan Q, Chu Y H, Rother A, Hawkridge M E, Maksymovych P, Yu P, Gajek M, Balke N, Kalinin, S V, Gemming S, Wang F, Catalan G, Scott J F, Spaldin N A, Orenstein J and Ramesh R 2009 *Nat. Mater.* **8** 229
[31] Nelson C T, Winchester B, Zhang Y, Kim S J, Melville A, Adamo C, Folkman C M, Baek S H, Eom C B, Schlom D G, Chen L Q and Pan X Q 2011 *Nano Lett.* **11** 828
[32] Gao W P, Addiego C, Wang H, Yan X X, Hou Y S, Ji D X, Heikes C, Zhang Y, Li L Z, Huyan H, Blum T, Aoki T, Nie Y F, Schlom D G, Wu R and Pan X Q 2019 *Nature* **575** 480
[33] Wu H J, Zhang Y, Wu J G, Wang J and Pennycook S J 2019 *Adv. Funct. Mater.* **29** 1902911
[34] Zeches R J, Rossell M D, Zhang J X, *et al.* 2009 *Science* **326** 977
[35] Li F, Lin D B, Chen Z B, Cheng Z X, Wang J L, Li C C, Xu Z, Huang Q W, Liao X Z, Chen L Q, Shrout T R and Zhang S J 2018 *Nat. Mater.* **17** 349
[36] Tao H, Wu H J, Liu Y, Zhang Y, Wu J G, Li F, Lyu X, Zhao C L, Xiao D Q, Zhu J G and Pennycook S J 2019 *J. Am. Chem. Soc.* **141** 13987
[37] Zhang N, Zheng T, Li N, Zhao C L, Yin J, Zhang Y, Wu H J, Pennycook S J and Wu J G 2021 *ACS Appl. Mater. Interfaces* **13** 7461
[38] Zhao C L, Wu H J, Li F, Cai Y Q, Zhang Y, Song D S, Wu J G, Lyu X, Yin J, Xiao D Q, Zhu J G and Pennycook S J 2018 *J. Am. Chem. Soc.* **140** 15252
[39] Fu H X and Bellaiche L 2003 *Phys. Rev. Lett.* **91** 257601
[40] Naumov I I, Bellaiche L and Fu H X 2004 *Nature* **432** 737
[41] Yadav A K, Nelson C T, Hsu S L, Hong Z, Clarkson J D, Schleputz C M, Damodaran A R, Shafer P, Arenholz E, Dedon L R, Chen D, Vishwanath A, Minor A M, Chen L Q, Scott J F, Martin L W and Ramesh R 2016 *Nature* **534** 138
[42] Das S, Tang Y L, Hong Z, *et al.* 2019 *Nature* **568** 368
[43] Wang Y J, Feng Y P, Zhu Y L, Tang Y L, Yang L X, Zou M J, Geng W R, Han M J, Guo X W, Wu B and Ma X L 2020 *Nat. Mater.* **19** 881

[44] Jeong C, Lee J, Jo H, Oh J, Baik H, Go K J, Son J, Choi S Y, Prosandeev S, Bellaiche L and Yang Y 2024 *Nat. Commun.* **15** 3887

[45] Dong G H, Li S Z, Li T, *et al.* 2020 *Adv. Mater.* **32** 2004477

[46] Fu Z Q, Chen X F, Li Z Q, Hu T F, Zhang L L, Lu P, Zhang S J, Wang G S, Dong X K and Xu F F 2020 *Nat. Commun.* **11** 3809

[47] Liu Y X, Qu W B, Thong H C, Zhang Y, Zhang Y F, Yao F Z, Nguyen T N, Li J W, Zhang M H, Li J F, Han B, Gong W, Wu H J, Wu C F, Xu B and Wang K 2022 *Adv. Mater.* **34** 2202558

[48] Wang H, Wu H J, Chi X, Li Y Y, Zhou C H, Yang P, Yu X J, Wang J, Chow G M, Yan X, Pennycook S J and Chen J S 2022 *ACS Appl. Mater. Interfaces* **14** 8557

[49] Li J L, Qu W B, Daniels J, Wu H J, Liu L J, Wu J, Wang M W, Checchia S, Yang S, Lei H B, Lv R, Zhang Y, Wang D Y, Li X X, Ding X D, Sun J, Xu Z, Chang Y F, Zhang S J and Li F 2023 *Science* **380** 87

[50] Wu H J, Ning S C, Waqar M, Liu H J, Zhang Y, Wu H H, Li N, Wu Y, Yao K, Lookman T, Ding X D, Sun J, Wang J and Pennycook S J 2021 *Nat. Commun.* **12** 2841

[51] Gao P, Yang S Z, Ishikawa R, Li N, Feng B, Kumamoto A, Shibata N, Yu P and Ikuhara Y 2018 *Phys. Rev. Lett.* **120** 267601

[52] Li L Z, Cheng X X, Jokisaari J R, Gao P, Britson J, Adamo C, Heikes C, Schlom D G, Chen L Q and Pan X Q 2018 *Phys. Rev. Lett.* **120** 137602

[53] Waqar M, Wu H J, Ong K P, Liu H J, Li C J, Yang P, Zang W J, Liew W H, Diao C Z, Xi S B, Singh D J, He Q, Yao K, Pennycook S J and Wang J 2022 *Nat. Commun.* **13** 3922

[54] Liu H J, Wu H J, Ong K P, Yang T N, Yang P, Das P K, Chi X, Zhang Y, Diao C Z, Wong W K A, Chew E P, Chen Y F, Tan C K I, Rusydi A, Breese M B H, Singh D J, Chen L Q, Pennycook S J and Yao K 2020 *Science* **369** 292

[55] Li N, Zhu R X, Cheng X X, Liu H J, Zhang Z Y, Huang Y L, Chu Y H, Chen L Q, Ikuhara Y and Gao P 2021 *Scripta Mater.* **194** 113624